

3 A MIX OF HALIDES

REDUCED BARRIER FOR ION MIGRATION IN MIXED $\text{MAPb}(\text{Br}_x\text{I}_{1-x})_3$ PEROVSKITES

Halide alloying in metal halide perovskites is a useful tool for optoelectronic applications requiring a specific bandgap. However, mixed-halide perovskites show ion migration in the perovskite layer, leading to phase segregation and reducing the long-term stability of the devices. Here, we study the ion migration process in methylammonium-based mixed-halide perovskites with varying ratios of bromide to iodide. We find that the mixed-halide perovskites show two separate halide migration processes, in contrast to pure-phase perovskites which only show a unique halide migration component. Compared to pure-halide perovskites, these processes have lower activation energy, facilitating ion migration in mixed versus pure-phase perovskites, and have a higher density of mobile ions. Under illumination, we find that the concentration of mobile halide ions is further increased and notice the emergence of a migration process involving methylammonium cations. Quantifying the ion migration processes in mixed-halide perovskites shines light on the key parameters allowing the design of bandgap-tunable perovskite solar cells with long-term stability.

This chapter is based on the following publication¹⁰⁴:
Lucie McGovern, Gianluca Grimaldi, Moritz H. Futscher, Eline M. Hutter, Loreta A. Muscarella, Moritz C. Schmidt, Bruno Ehrler, "Reduced Barrier for Ion Migration in Mixed-Halide Perovskites", *ACS Applied Energy Materials*, vol. 4, no. 12, pp. 13431–13437, 2021.

3.1 INTRODUCTION

Perovskite solar cell efficiencies have increased rapidly in the past decade and now reach an impressive 25.5 % power conversion efficiency in single-junction cells, closely matching up with the 26.7 % record for silicon solar cells¹⁰. On top of these high efficiencies, another key advantage with perovskites lies in the bandgap tunability of the material, easily achievable through mixing of the A, B, and X elements composing the ABX_3 perovskite structure¹¹. For example, halide alloying has been shown to allow for a large variation in the bandgap, from 1.6 eV to 3.2 eV in methylammonium-based $MAPbX_nY_{3-n}$ perovskites - with (X,Y) consisting of either I, Br, or Cl. The main factor impeding large-scale commercialization of perovskite devices remains the issue of their stability in time, with only a handful of perovskite devices showing the necessary stability under accelerated lifetime conditions. In that regard, the more intrinsically stable the perovskite layer, the easier it will be to stabilize the full devices.

For mixed-halide systems, the instability is commonly observed through the photoinduced phase segregation process, in which light induces de-mixing of the perovskite composition, leading to the formation of iodide-rich and bromide-rich phases within the film¹⁰⁵. Photoinduced phase segregation relies on the migration of the halide species through the perovskite film, linking it to the larger topic of ion migration in perovskite solar cells. At its core, ion migration is a process by which ions from the lead halide $APbX_3$ structure become mobile and hop through the perovskite lattice. This leads to long-term stability issues, as the process might not be fully reversible^{106–108}. Combining bandgap tunability with long-term stability is crucial for the further development of perovskite devices. To this end, a better understanding of the ion migration process in mixed-halide systems is needed, to determine specific parameters of influence that can aid to mitigate or suppress this feature altogether.

During illumination, the observation of halide ion migration is easily accessible through monitoring of the photoinduced phase segregation, using UV/visible absorption, PL emission spectroscopy and/or transient absorption spectroscopy^{69,109–115}. In the absence of segregation however, which is the case when the cells are in the dark or when the mixing ratio

of bromide to iodide falls below the 0.2 threshold¹⁰⁵, we need other tools to characterize the ion migration processes at play. So far there have only been a limited number of studies focussing on these regimes, using AC impedance spectroscopy or DC polarisation measurements^{116,117}. While these works shed light on ion migration in mixed-halide perovskites, the full picture remains elusive, specifically whether the trends observed stem from iodide or bromide migration, and how to attribute the relative contributions to the ion migration process, in terms of migration activation energy, ion diffusion coefficient and concentration of mobile ions.

Transient Ion Drift (TID) can be used for ion migration measurements in dark as well as in light conditions, and provides a detailed description of the process, revealing the nature of the mobile ion (whether anion or cation), and allowing for the quantification of the activation energy E_a , diffusion coefficient D_{ion} and concentration N_{ion} of mobile ions^{51,118}. With this work, we aim to answer the following questions: i) how does the mixing ratio of bromide to iodide change the ion migration process for the perovskite devices; ii) how does light affect this ion migration process. To answer these questions, we prepare perovskite solar cells with varying ratios of bromide to iodide, measure the TID capacitance transients in these devices, and finally fit these transients in order to extract the ion migration characteristics E_a , D_{ion} and N_{ion} of the various mixed-halide perovskite compositions.

3.2 RESULTS AND DISCUSSION

3.2.1 MIXED-HALIDE SOLAR CELL FABRICATION

In order to study the effect of bromide to iodide ratio on the ion migration process, we prepare solar cell devices with the composition $\text{MAPb}(\text{Br}_x\text{I}_{1-x})_3$, and vary the x ratios ($x = 0.1, 0.2, 0.5$ and 0.7) following a synthesis described in Section 3.4.1. For reliable comparison with our previously-published pure halide devices^{56,76}, we use the same device structure (see Figure 3.1a). To characterize these devices, the dark IV curves are presented in Figure 3.1b. These curves show a hysteretic behaviour for most of the solar cells considered, an effect typically associated with the formation of interfacial charges between the perovskite and the transport materials⁸⁹. The main requirement for successful TID characterisation is a low series resistance, so that the measured signal can be related to the capacitance of the perovskite when a small AC voltage is applied. The series resistance is determined by fitting the Nyquist

plots (see Section 3.4.2) and is found to be below $20 \Omega \text{ cm}^2$ throughout the bromide to iodide ratios used in this study. The dark IV curves presented here are consistent with those found in the literature for devices with similar perovskite and transport materials²⁹.

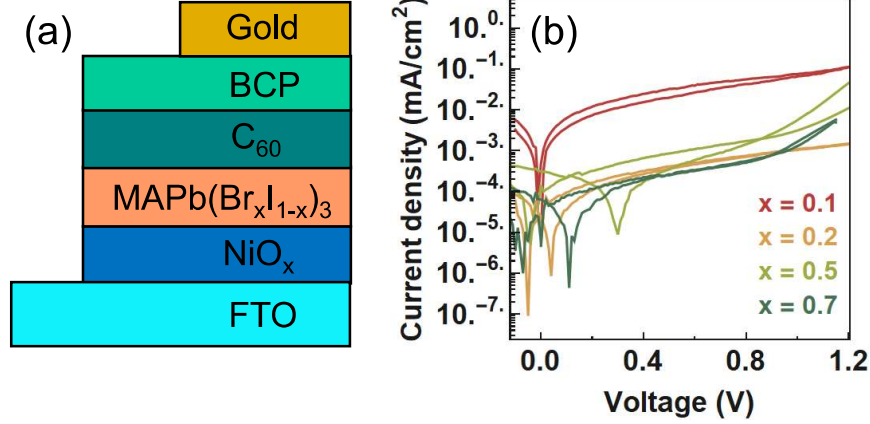


FIGURE 3.1. a P-i-n device architecture of the $\text{MAPb}(\text{Br}_x\text{I}_{1-x})_3$ perovskite solar cells, using $x = 0.1, 0.2, 0.5$ and 0.7 , and their corresponding (b) dark-IV curves measured with a scan speed of 10 mV s^{-1} , presented on a semi-log scale.

3.2.2 CAPACITANCE MEASUREMENTS OF THE MIXED-HALIDE SOLAR CELLS

TID is an electronic spectroscopy technique aimed at characterising ion migration processes in semiconductor devices^{51,118}. We measure the capacitance transients of the $\text{MAPb}(\text{Br}_x\text{I}_{1-x})_3$ perovskite solar cells at different temperatures after applying a voltage pulse of 1.5 V for 2 s (see Section 3.4.2). We note that we choose the 1.5 V voltage pulse such that it is both high enough to detect the ion dynamics with TID (see the comparison with TID after application of voltage biases of 1 V or 1.25 V in Section 3.4.2) while remaining below the threshold for electrically-induced phase segregation^{119,120}. The results are plotted in Figure 3.2 as the relative difference in capacitance, i.e. $\Delta C = C(t) - C_0$, with $C(t)$ the capacitance as a function of time and C_0 the capacitance at time $t = 0$. These transients already provide a qualitative picture of ion migration in these mixed-halide perovskite systems. In dark, we find that the capacitance decays for all the halide ratios considered. In p-type perovskites, negative capacitance transients are associated with migration

from an anion species. Since the only negatively charged species in ABX_3 is the X^- halide ion, this signals migration of a halide species. This assignment is similar to what we have previously found in both pure-halide perovskites, $MAPbI_3$ and $MAPbBr_3$ ^{56,76}. Note that the doping of the perovskite layer is a matter of active debate (assigned to n-type¹²¹, p-type¹²² and intrinsic¹²³). The observed feature could thus correspond to halide migration, but other assignments remain possible (cation or halide vacancy migration in an n-type material, cation vacancy migration in p-type material). The negative feature observed here shares many properties with halide migration observed directly^{42,49}, and we hence assign it to halide migration for the remainder of the discussion. For $x = 0.1$, there is a small positive signal visible for the highest temperatures, at 315 K and 330 K, but this positive trend remains very small compared to the main negative trend observed. We additionally measure the capacitance transients under illumination for $x = 0.1$ and 0.2. The devices with $x = 0.5$ and 0.7 could not be measured during illumination, because the light-induced phase segregation would change the sample in a non-reversible way during the capacitance measurements. The results under illumination show a different picture than those in the dark, where on top of the negative transient present at all temperatures, a new positive trend becomes clearly visible after 100 to 200 milliseconds, for the whole temperature range considered. Since we are considering p-type perovskites, we attribute this positive trend to cation migration. As lead migration is energetically unfavourable³³, we assign the feature to methylammonium cation migration. Finally, we also observe a general growth in the magnitude of the negative capacitance transients compared to dark conditions. Under light conditions, the relative capacitance difference is highest for $x = 0.2$, with $\Delta C = -10 \text{ nF cm}^{-2}$.

3.2.3 QUANTIFICATION OF ION MIGRATION CHARACTERISTICS

To obtain a more quantitative picture of the ion migration process, we fit the TID capacitance transients to the following Equation:

$$C(t, T) = C_\infty(T) + \sum_n \Delta C_n(T) \exp \left(\frac{-t}{p_{fit(n)} T \exp \left(\frac{E_{a(n)}}{k_B T} \right)} \right) \quad (3.1)$$

where $C(t, T)$ is the capacitance as a function of time and temperature, $C_\infty(T)$ is the steady-state value of the capacitance at a certain temperature T , $\Delta C_n(T)$ is the capacitance magnitude at temperature

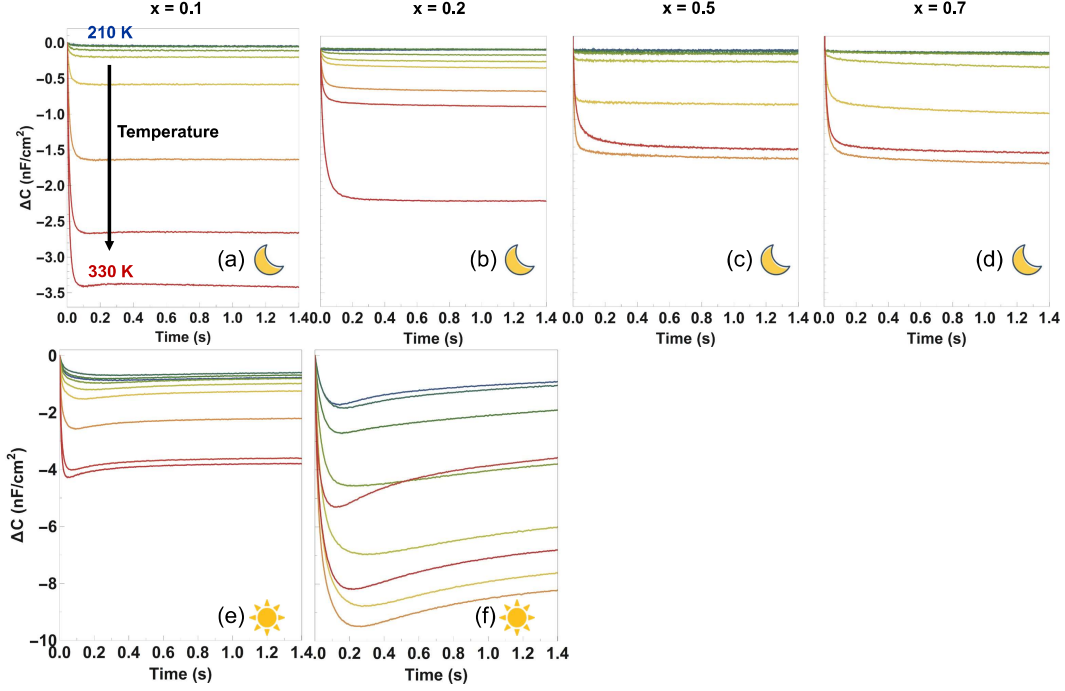


FIGURE 3.2. Relative difference in capacitance transients $\Delta C = C(t) - C_0$ of the $\text{MAPb}(\text{Br}_x\text{I}_{1-x})_3$ solar cells, measured with an AC voltage of 20 mV, after applying a voltage pulse of 1.5 V for 2 seconds, under dark conditions, for (a) $x = 0.1$, (b) $x = 0.2$, (c) $x = 0.5$ and (d) $x = 0.7$, and during illumination, for (e) $x = 0.1$, (f) $x = 0.2$. The transients shown here are taken at temperatures of 210 K, 225 K, 240 K, 255 K, 270 K, 285 K, 300 K, 315 K and 330 K. Light conditions correspond to a 405 nm CW laser shining directly on the considered pixel, with a power density of 1.59 W cm^{-2} .

T of the process n , $p_{fit(n)}$ is a fitted parameter for process n that depends on the diffusion coefficient, and $E_{a(n)}$ is the activation energy of the process n . Every migration pathway would correspond to an individual exponential decay, and for the mixed-halide perovskites we can fit the data with two or three decay traces, respectively under dark and illumination conditions.

The fit is obtained by using a global fit algorithm as described in Section 3.4.3. The values obtained for the ion migration activation energy, ion diffusion coefficient and density of mobile ions are shown in Figure 3.3. For comparison, we add the values for MAPbI_3 and MAPbBr_3 , reproduced from references [56, 76]. When fitting the capacitive transients, we find that we need 2 exponential contributions to correctly fit the negative peak, whether in dark or in light, and across the full composition range

from $x = 0.1$ to $x = 0.7$. This means that for methylammonium-based mixed-halide perovskites, there are 2 halide migration processes at play, either from the iodide and the bromide species, or from the combination of a grain boundary process with a bulk process, similar to what we have previously observed for MAPbBr₃ cells with varying grain size¹²⁴. This is in stark contrast with the single halide migration process happening in the pure-phase halide perovskites. The small positive peak present in dark for $x = 0.1$ is too low to be fitted, suggesting that the concentration of mobile methylammonium ions in this case is below 10^{14} cm^{-3} (considering the hypothesis of a high doping density of 10^{17} cm^{-3} , see Sections 3.4.2 and 3.4.3). To fit the capacitance transients taken under illumination, 3 exponential contributions are used, where 2 are assigned to the negative halide peak, and 1 to the positive methylammonium peak.

ION MIGRATION UNDER DARK CONDITIONS Looking at Figure 3.3a, we notice that both activation energies from the halide migration process are decreased in mixed-halide compositions compared to the single ion migration activation energies from the pure-halide compositions. Specifically, for the first process contributing to halide migration - with highest activation energy, labelled Halide (1) in Figure 3.3 - the activation energy is most decreased in the low-bromide regime, with $E_a = 157 \pm 3 \text{ meV}$ for $x = 0.1$ and $E_a = 98 \pm 7 \text{ meV}$ for $x = 0.2$, then increases to $E_a = 289 \pm 10 \text{ meV}$ for $x = 0.5$ and $E_a = 217 \pm 11 \text{ meV}$ for $x = 0.7$. The trend is similar for the second process contributing to halide migration - with lower activation energy, labelled Halide (2) in Figure 3.3 - with a maximal value of $E_a = 139 \pm 14 \text{ meV}$ for $x = 0.5$. García-Rodríguez *et al.*¹¹⁶ show an increase in the activation energy with higher bromide concentration, in their case using bromide concentrations below 10 %. Here, we find that halide migration has a lower activation energy in mixed devices for bromide contents of 10, 20, 50 and 70 %.

Figure 3.3b shows the halide diffusion coefficients in the dark. The diffusion coefficient of both contributions is constant for different bromide concentrations. The diffusion coefficient of Halide (1) is on the order of 10^{-9} to $10^{-10} \text{ cm}^2 \text{ s}^{-1}$, similar - within the error bar - to the iodide and bromide diffusion coefficients in MAPbI₃ and MAPbBr₃. Halide (2) on the other hand is slower, on the order of $10^{-11} \text{ cm}^2 \text{ s}^{-1}$. Halide migration is thus equally fast in all the mixed devices.

Figure 3.3c shows the density of mobile halide ions. The Halide (2) peak has a relatively constant and similar concentration to the bromide and iodide mobile ion densities found in the pure-phase perovskites. The

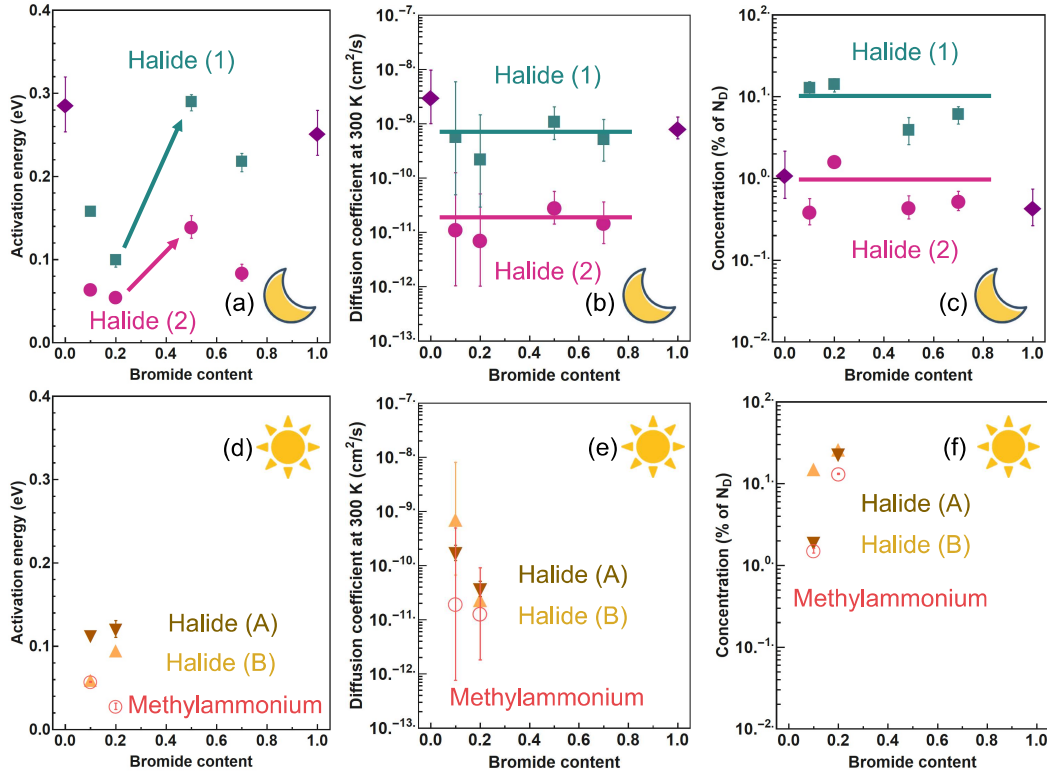


FIGURE 3.3. Comparison of the characteristics of ion migration as a function of the bromide to iodide ratio. Halide ion migration characteristics in dark, with (a) ion migration activation energies, (b) halide ion diffusion coefficients at 300 K, and (c) concentration of mobile halide ions, represented as a fraction of the doping density. The two migration processes Halide (1) and Halide (2) are shown in blue and pink, respectively. The arrows in (a) represent the point of phase transition, the lines in (b) and (c) are a guide to the eye representing the weighted averages for diffusion coefficient and mobile ion concentration. The halide and methylammonium ion migration characteristics in light are respectively shown in dark and light orange - Halide (A) and Halide (B) - and in red, with (d) ion migration activation energies, (e) halide and methylammonium ion diffusion coefficients at 300 K, and (f) concentration of mobile ions. Error bars represent the standard deviation of the fit parameters from several fits giving lowest chi-square values (see Section 3.4.3). The values for $x = 0$ and $x = 1$ are reproduced from references [56, 76].

peak for Halide (1) on the other hand shows a clear increase in the concentration of migrating halide ions compared to the pure-phase cases, with up to 10 % of the doping density for the devices with 10 % and 20 % bromide concentrations. There is thus more halide migration in the mixed devices.

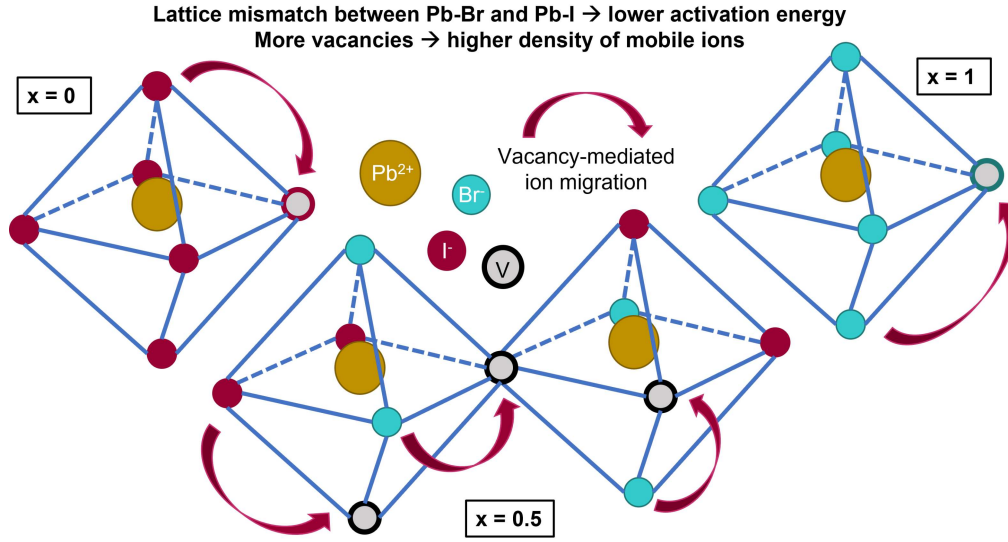


FIGURE 3.4. Schematic picture of the ion migration process in the pure-halide perovskites compared to the mixed-halide perovskites. The lattice mismatch between the bromide and iodide perovskite lattices in the mixed-halide case leads to a decreased activation energy for the migration step. The number of vacancies is also higher for the mixed-halide case, thereby increasing the density of mobile halide ions in the mixed-halide perovskites.

ILLUSTRATIVE SCHEME One possible scheme to rationalise these observations is to consider the two processes separately. Halide (1) shows a high density of ions which presumably arises from an increased density of vacancies when moving from pure-halide to mixed-halide compositions. The difference in solubility of iodide and bromide species has indeed been suggested to result in heterogeneous nucleation during thin-film deposition¹²⁵ and has led to the observation of lower crystallinity in the mixed films¹²⁶, which could in turn lead to an increase in the density of halide vacancies. The Halide (1) process would thus become more prominent for mixed-halides due to the higher number of vacancies. This is in line with the finding that the fraction of halide vacancies enables and controls the rate of phase segregation^{40,110}. Overall, the Halide (1) process shares many features with the halide migration in pure-halide perovskites. It has a similar diffusion coefficient and a slightly reduced activation energy, especially for the mixing ratios $x < 0.2$. This reduction in activation energy could be associated with the strain in the crystal from the different bond length between bromide and iodide¹²⁷, in which case the activation energy should be lowest close to the phase transition. A reduced activation energy might naively lead to an increase diffusion coefficient. However, in the mixed halide perovskites the entropy is likely to decrease

when the ion is moving, since it is most likely coming from a well-mixed unit cell. The effect would be accentuated if the ions are moving towards a transport layer, as the mobile halide will accumulate there and likely end up in a unit cell enriched in one of the halides. The maximal entropy difference for a mobile halide ion to migrate is the entropy difference $\Delta S = k \ln \frac{8!}{4! \times 4!} = 3.6 \times 10^4 \text{ eV K}^{-1}$, where the argument of the logarithm represents the ratio between the number of possible configurations for the neighbours of an ion in a mixed-halide phase of $x = 0.5$ (i.e. $\frac{8!}{4! \times 4!}$) and the number of configurations for neighbouring ions in a single-halide phase (i.e. 1). While we expect this effect to be large in the well-mixed perovskites ($x < 0.2$), the higher bromide ratios already show some de-mixing even in the dark and when a bias is applied^{128,129}, which means that the entropy change during migration towards the interfaces is smaller. Taken together, the reduced activation energy and entropy gain appear to balance each other, resulting in a rather constant diffusion coefficient at room temperature. A representation of this scheme is depicted in Figure 3.4.

Halide (2) represents a very slow ion with a low activation energy. The diffusion coefficient is about 2 orders of magnitude lower than that of Halide (1). Presumably, even if present, this process cannot be detected easily in pure-halide mixtures as also the concentration is about 2 orders of magnitude lower than Halide (1). We speculate that a similar process could be responsible for the very slow dynamics (minutes to days) often seen in perovskite devices¹³⁰. The observation of the difference in the activation energy for migration before and after the $x = 0.2$ mark - with much lower migration barriers for the perovskites with low-bromide content - is also noteworthy. The $x \geq 0.2$ threshold marks the onset of light-induced phase segregation in mixed-halide perovskites and is thought to arise due to the phase transition (from tetragonal to cubic) close to this composition. Here this threshold is clearly visible in the ion migration properties of the devices, reinforcing the relationship between perovskite composition, phase segregation and ion migration instability.

ION MIGRATION UNDER ILLUMINATION When comparing halide migration in dark and in light, we find that the activation energy is decreased in light, see for instance for the perovskite with 10 % bromide, the small decrease from $65 \pm 5 \text{ meV}$ to $60 \pm 3 \text{ meV}$ for the first peak, and the larger decrease from $157 \pm 3 \text{ meV}$ to $113 \pm 4 \text{ meV}$ for the second peak. This is consistent with our previous work on these systems¹¹⁵. We note that the similar activation energies between Halide (1) and Halide (A) seem to

suggest the same process, but that TID cannot distinguish mechanisms, complicating the assignments of the Halide (1) and Halide (2) peaks in light. We thus choose the nomenclature Halide (A) and Halide (B) for the halide migration peaks in light. When comparing the diffusion coefficients in dark and in light, no clear trend seems to emerge as there is both an increase in one of the features, and a decrease in the other. The most noticeable difference lies in the concentration of mobile halide ions, with a clear increase in the total halide concentration as a function of doping density, from 12.8 % to 17.3 % for $x = 0.1$, and from 15.4 % to 36.9 % for $x = 0.2$. Under light, there is thus an increased halide ion migration, partly due to a lower activation energy, and mostly due to the much larger fraction of mobile halide ions. We note that at such high densities the quantification of ion migration by TID might not be accurate anymore because the analysis method assumes that the change in the charge density from mobile ions is small compared to the background doping density.

As mentioned above, in the presence of light, a new cation migration process appears for the devices with $x = 0.1$ and $x = 0.2$, on top of the halide migration process. This process has a very low activation energy (< 0.060 eV), has a low diffusion coefficient on the order of 10^{-11} cm² s⁻¹, and is prominent, representing 1.5 % and 13.2 % of the doping density, respectively for the devices with 10 % and 20 % bromide concentrations. So far in dark, we have only observed MA⁺ migration in the case of the pure MAPbI₃ perovskite, and in this work as a minor contribution to the MAPbBr_{0.3}I_{2.7} perovskite. In other words, the higher the bromide concentration, the more methylammonium migration is suppressed, as the bond between lead and halide gets stronger. Under light conditions, it thus seems like the barrier preventing cation migration is released, in agreement with galvanostatic measurements from Zhao *et al.*¹³¹ showing decreased activation energies with increasing light intensity. This effect might happen either through an increase in the number of MA⁺ vacancies in light -similar to the increase of halide vacancies observed in light¹³²- and/or through a loosening of the Pb-X bond, perhaps upon polaron formation^{133,134}. We also note that one of the theories behind light-induced phase segregation involves polaron stabilization of the iodide domains. One possibility is that halide migration might promote this effect, while cation migration might prevent it: there, the reduction (or suppression) of cation migration in light when $x > 0.2$ would help rationalize the $x = 0.2$ threshold observed in light-induced phase segregation. This calls for future investigation.

All in all, light thus has two effects on the ion migration process for the mixed-halide perovskites: first, it increases the number of mobile halide ions; second, it introduces an extra cation migration pathway. These results are in line with the previous work from Kim *et al.*¹¹⁷, showing increased ionic conductivity in light compared to dark for similar perovskite compositions. In conductivity measurements, however, the contributions from diffusion coefficient and mobile ion density cannot be disentangled: here, we can thus specifically attribute the increased ion migration in light to an increase in the mobile ion density.

3.3 CONCLUSION

In conclusion, we find that mixing iodide and bromide in MAPb(Br_xI_{1-x})₃ solar cells facilitates halide ion migration by decreasing the activation energy and by increasing the number of mobile halide ions. We also notice the appearance of a second pathway in the halide ion migration process, not observed in the pure-phase perovskites. In light, the density of mobile halide ions increases even more, and additional migration from the methylammonium cation becomes prominent. To reduce ion migration in mixed-halide perovskites, it is thus essential to increase the activation energy of the process and/or to decrease the density of mobile halide ions. These can be achieved for instance by reducing the unit cell size by replacing MA⁺ with Cs⁺ (E_a increase)¹¹⁵, or by tailoring the Pb:X stoichiometry to reduce the number of halide vacancies (N_{ion} decrease)¹²². Our quantitative assessment of the ion migration processes in mixed-halide perovskites thus provides new insights into the relative contributions of activation energy, ion diffusion and mobile ion density, tracing the path towards rational design of mitigation strategies, necessary for long-term stability of bandgap-tunable perovskite solar cells.

3.4 APPENDIX

3.4.1 SOLAR CELL DEVICE FABRICATION

The substrates are laser-patterned Fluorinated Tin Oxide (FTO)-coated glass substrates. We clean them with 3 successive rounds of sonication of 15 minutes each, in deionized water, acetone, and isopropanol; and further plasma clean them for 20 minutes at 100 W.

The NiO_x Hole Transport Layer (HTL) is prepared by dissolving the precursor (nickel(II) acetylacetonate, Sigma Aldrich) in ethanol at a concentration of 0.3 M. The solution is then filtered with a PTFE membrane of diameter $0.45\text{ }\mu\text{m}$, and then spin coated on the cleaned FTO glass at 4000 rpm for 15 seconds. The as-prepared film is dried at $150\text{ }^\circ\text{C}$ for 1 minute and then annealed with a slow heating rate of $3\text{ }^\circ\text{C}/\text{min}$ until a temperature of $350\text{ }^\circ\text{C}$ is reached. The samples are then left at $350\text{ }^\circ\text{C}$ for 1 h, and further plasma cleaned for 20 minutes at 100 W before the perovskite spin coating step.

The perovskite synthesis has been previously described in reference [114] and goes as follows. To prepare the perovskite solutions, we first mix DMF and DMSO in a 4 : 1 (DMF:DMSO) volume ratio. We then dissolve PbI_2 (TCI, 99.99 %, trace metals basis), $\text{CH}_3\text{NH}_3\text{I}$ (TCI, > 99 %), PbBr_2 (Sigma-Aldrich, trace metals basis), and $\text{CH}_3\text{NH}_3\text{Br}$ (TCI, > 98 %) precursors in this solvent mixture, with molar ratio of 1.1 M. These stock solutions are then mixed (PbI_2 with $\text{CH}_3\text{NH}_3\text{I}$, and PbBr_2 with $\text{CH}_3\text{NH}_3\text{Br}$) to obtain MAPbI_3 and MAPbBr_3 solutions, using a 1 : 1 molar stoichiometric ratio. The $\text{MAPb}(\text{Br}_x\text{I}_{1-x})_3$ precursor solutions are then prepared by mixing x parts MAPbBr_3 stock solution with $(1 - x)$ parts MAPbI_3 stock solution, resulting in 1.1 M $\text{MAPb}(\text{Br}_x\text{I}_{1-x})_3$ solutions. The perovskite films are prepared by spin coating the precursor solutions onto the NiO_x -coated FTO substrates, with a spin speed of 9000 rpm for 30 s. The chlorobenzene (Sigma-Aldrich, anhydrous, $\geq 99\%$) anti-solvent is dropped 15 s after the start of spin coating. The film is then annealed at $100\text{ }^\circ\text{C}$ for 1 h.

We note that the devices with pure MAPbI_3 and pure MAPbBr_3 were prepared in a similar fashion, with only a few differences: the MAPbI_3 solution has a concentration of 1.35 M in pure DMF, and is spin coated for 25 seconds at 5000 rpm, with addition of the chlorobenzene anti-solvent after 5 seconds; the MAPbBr_3 solution is spin coated at 6000 rpm for 30 seconds.

The C_{60} and BathoCuProine (BCP) Electron Transport Layers

(ETL), as well as the gold electrode are thermally evaporated: 30 nm of C_{60} (0.2 \AA s^{-1} rate), 8 nm of BCP (0.2 \AA s^{-1} rate) and 120 nm of gold (0.1 \AA s^{-1} for the first 10 nm, then 1.0 \AA s^{-1} for the remaining 110 nm). The pressure remained below 8×10^{-6} mbar during all thermal evaporation steps. The preparation and spin coating of the perovskite solutions are done in a nitrogen-filled glovebox, while the spin coating of NiO_x is done in a downflow cabinet.

An example SEM image of the as-prepared $MAPbBr_{1.5}I_{1.5}$ perovskite film is shown below (Figure 3.5), with apparent grains of size 300 nm to 1 μm . SEM imaging was done using a FEI Verios 460 instrument. The perovskite film thicknesses are measured by profilometry, using a KLA Tencor stylus profiler P7 instrument.

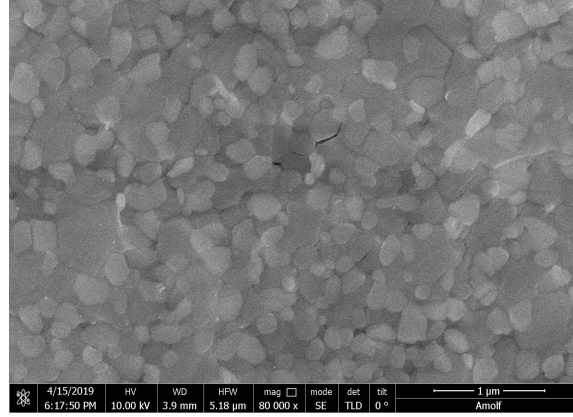


FIGURE 3.5. SEM image of the $MAPbBr_{1.5}I_{1.5}$ perovskite film, showing a flat and homogeneous layer with features between 300 nm and 1 μm .

We have previously published the PL spectra, absorption spectra and XRD diffractograms of the $MAPb(Br_xI_{1-x})_3$ films prepared by this synthesis recipe¹¹⁴. These measurements confirm that the films have a comparable and controlled quality for the whole range of x-ratios used. From the absorption spectra and XRD diffractograms we observe that both the bandgap and the unit cell size scale with the x-ratio, and that on a macroscopic level, the halides are homogeneously mixed. Finally, the peaks around 15 and 30 degrees observed in XRD for $0.25 < x < 1$ have similar FWHM, reflecting the constant trend in grain size for these films.

In the full devices, we note that we choose the same device structure as our previously-published pure halide devices^{56,76}. In this context, NiO_x and C_{60} / BCP are chosen specifically with the aim of avoiding ion migration from the transport layers themselves – a process commonly reported for traditional HTL and ETL such as Spiro-OMeTAD¹³⁵ and

TiO₂¹³⁶. We can thus safely assume that the effects observed in this study stem from the perovskite layers themselves.

To observe the effect of illumination on the ion migration properties of the mixed-halide devices, we use the following illumination conditions: a 405 nm CW laser is focused on the considered pixel, using a 1 mW beam and a spot size of $6.3 \times 10^{-4} \text{ cm}^2$, amounting to a power density of 1.59 W cm^{-2} .

3.4.2 ELECTRICAL MEASUREMENTS

The TID technique has been extensively described elsewhere^{51,118}. To resolve the Equation for the ion diffusion coefficient (see Equation 3.1), we need both the perovskite permittivity ϵ and the doping density N_D of the film. We get these by performing Capacitance versus Voltage (CV) measurements, as shown in Figure 3.6. These show $\epsilon = 38.6$ and $N_D = 1.98 \times 10^{16} \text{ cm}^{-3}$ for the MAPbBr_{1.5}I_{1.5} film, above the threshold for experimentally accessible charge densities for the perovskite film thicknesses considered here, as defined by Kirchartz *et al.*¹³⁷. For $x = 0.7$, we use $\epsilon = 17.2$ and $N_D = 2.53 \times 10^{16} \text{ cm}^{-3}$ as determined by CV measurement. In the cases of $x = 0.1$ and $x = 0.2$, CV measurements were not conclusive in the determination of N_D , and we use instead the average found by combining the doping densities of the devices with $x = 0$, $x = 0.5$, $x = 0.7$, and $x = 1$, which is $4.39 \times 10^{16} \text{ cm}^{-3}$. To account for possible discrepancies in the determination of the diffusion coefficient - which is based on N_D - we consider a large error bar for N_D in these two cases, with a lower bound of 10^{16} cm^{-3} and an upper bound of 10^{17} cm^{-3} . This is reflected in the large error bars for the diffusion coefficient values as shown in Figure 3.3b,e.

To further characterize the cells, we perform Thermal Admittance Spectroscopy (TAS) on the MAPb(Br_xI_{1-x})₃ solar cells. The results shown in Figure 3.7 present a constant capacitance plateau in the intermediate frequency range, which spans from 10^2 Hz to $5 \times 10^4 \text{ Hz}$ for the devices with $x = 0.1$ and $x = 0.2$, and from $5 \times 10^3 \text{ Hz}$ to $5 \times 10^4 \text{ Hz}$ for the devices with $x = 0.5$ and $x = 0.7$. This region of constant capacitance is the region where we measure the geometric capacitance of the device, where capacitance is determined by the depletion capacitance. This is the reason why we choose a frequency of 10^4 Hz for all the TID measurements, within that region of interest. In light, we notice that the low-frequency regime, representative of ion movement back and forth close to the interfaces, increases drastically, with 4 orders of magnitude

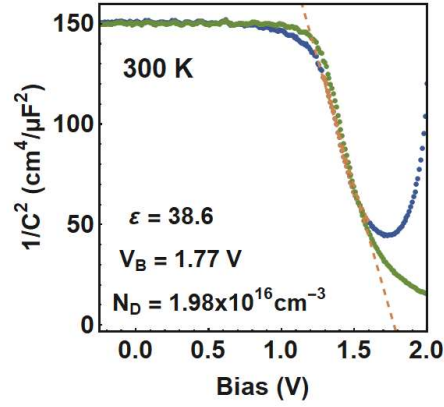


FIGURE 3.6. Typical capacitance versus voltage curve, measured at 300 K with a V_{AC} of 20 mV applied with a frequency of 10 kHz, here for the $\text{MAPbBr}_{1.5}\text{I}_{1.5}$ device. The forward and reverse scans are shown in green and blue, respectively.

difference. These high values are in line with previous works^{54,97}. The increase in capacitance values in the low-frequency regime when illuminating the devices has also been observed previously in TAS measurements of perovskite solar cells under light¹³⁸.

The phase angle part of the Bode plot is shown in Figure 3.8. At 10 kHz, the phase shift is close to -90° for all of the $\text{MAPb}(\text{Br}_x\text{I}_{1-x})_3$ devices, indicating that the devices are mostly capacitive (i.e. not resistive) at that frequency.

We further use the TAS measurement to determine the series resistance and parallel resistance of each of the devices, see Table I below. The methodology is the following: we fit the semi-circle of the Nyquist plot to an RC equivalent circuit model containing an RC circuit (with resistance and capacitance values R_p and C_p) in series with a resistor (with resistance R_s). The fit is performed in the region close to the TID measurement frequency of 10^4 Hz - here using a frequency range from 5×10^3 Hz to 5×10^4 Hz. This allows us to check that the series resistance is low enough for proper TID characterisation and it is the reason for the limited frequency range shown here. The resulting fits are shown in Figure 3.9. We observe that the very first datapoints seem to show a systematic error for most of the x -halide ratios (with the exception of $x = 0.5$), but we note that these datapoints are the points of highest frequency, where it is possible that the feature comes from another smaller semi-circle, representing an interfacial RC circuit in series to the main RC circuit modelled here¹³⁹.

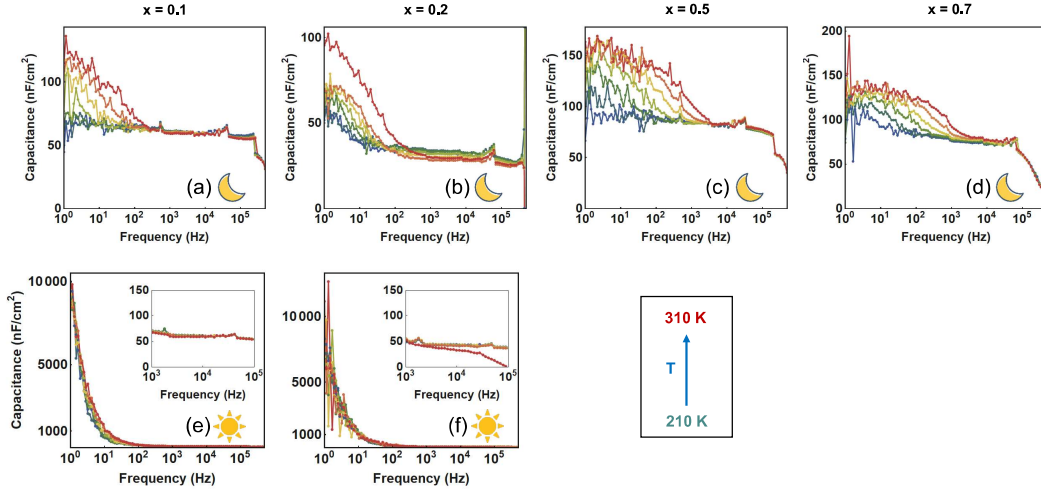


FIGURE 3.7. Impedance spectra of the $\text{MAPb}(\text{Br}_x\text{I}_{1-x})_3$ solar cells, measured from 1 Hz to 5×10^4 Hz with an AC voltage of 50 mV, in dark conditions, for (a) $x = 0.1$, (b) $x = 0.2$, (c) $x = 0.5$ and (d) $x = 0.7$; and in light conditions, for (e) $x = 0.1$, (f) $x = 0.2$. Insets in (e) and (f) allow for better visualization of the capacitance plateau at intermediate frequencies. The spectra shown here are taken at temperatures of 210 K, 230 K, 250 K, 270 K, 290 K and 310 K. Light conditions correspond to a 405 nm CW laser shining directly on the considered pixel, with a power density of 1.59 W cm^{-2} .

Light IV characterisation of the $\text{MAPb}(\text{Br}_x\text{I}_{1-x})_3$ solar cell devices is shown below in Figure 3.10. The devices show relatively low V_{OC} values of $(1.0 \pm 0.1) \text{ V}$. The FF and J_{SC} values are lower than literature values, due to the choice of transport layers. The device with $x = 0.7$ shows signs of phase separation, degrading the cell performance during the measurement timeframe itself. For TID characterisation of the devices with $x = 0.5$ and $x = 0.7$, we use fresh devices which have not been exposed to light, to avoid the light-induced phase separation process established for $x > 0.2$.

Some devices show shunting. The phase measurement in TAS shows that the measurement is mostly capacitive at the frequencies with which we measure TID (see Figure 3.8), ensuring that this shunting of the solar cells is not an issue for TID characterisation in this work.

We further note that for TID measurements, devices with non-optimal charge extraction could affect two parameters in the ion migration process, namely the mobile ion density, and the ion diffusion coefficient. However, the variation in these values is not expected to exceed one order of magnitude, and mobile ion densities and ion diffusion coefficients

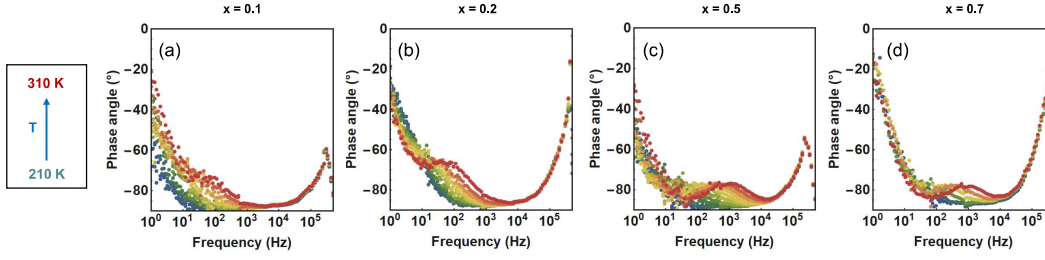


FIGURE 3.8. Phase shift in the Bode plot presentation of the impedance spectra of the $\text{MAPb}(\text{Br}_x\text{I}_{1-x})_3$ solar cells, measured from 1 Hz to 500 kHz with an AC voltage of 50 mV, in dark conditions, for (a) $x = 0.1$, (b) $x = 0.2$, (c) $x = 0.5$ and (d) $x = 0.7$.

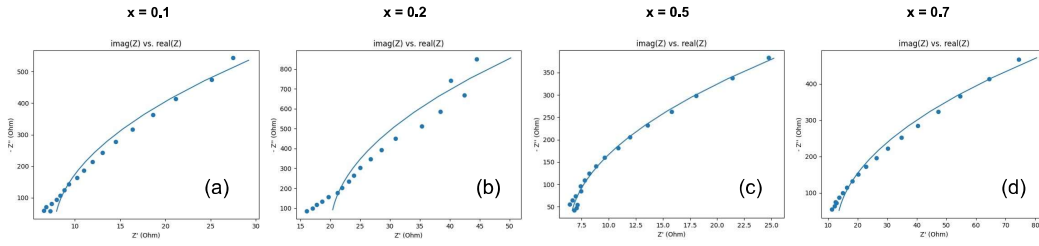


FIGURE 3.9. Fitting of the Nyquist semi-circle in the frequency range from 5 kHz to 50 kHz, at 300 K, for the $\text{MAPb}(\text{Br}_x\text{I}_{1-x})_3$ solar cells with (a) $x = 0.1$, (b) $x = 0.2$, (c) $x = 0.5$ and (d) $x = 0.7$.

are already presented with a high error bar in this manuscript. We thus conclude that the trends obtained with the present set of $\text{MAPb}(\text{Br}_x\text{I}_{1-x})_3$ devices would remain equivalent to that obtained with of a series of devices with optimized light IV characteristics.

We measure TID with different filling voltages (1 V, 1.25 V, 1.5 V). An example of the TID datasets with varying pulse voltages for the device with $x = 0.1$ is shown in Figure 3.11 below. There, we notice that the 1 V filling voltage is not sufficient for the TID measurement, as the built-in bias is on the upper end of that scale. We decide to base our analysis on the TID measurements taken with a voltage of 1.5 V, as it reliably offers the best signal when considering the range of device compositions measured for this study. Upon application of this 1.5 V bias, we assume that the depletion layer in the perovskite is fully collapsed. Note that we might see even larger signals for higher voltages, but the high injected current risks damage to the device. We account for this with the large error bar on the ion densities measured.

Composition	Series resistance ($\Omega \text{ cm}^2$)	Parallel resistance ($\Omega \text{ cm}^2$)	Capacitance (nF)
$x = 0.1$	7.72 ± 0.75	13400 ± 1300	58 ± 0.1
$x = 0.2$	20.06 ± 1.24	24400 ± 2700	36 ± 0.1
$x = 0.5$	6.41 ± 0.48	7760 ± 540	82 ± 0.2
$x = 0.7$	12.95 ± 0.84	3400 ± 100	65 ± 0.2

TABLE I. Values for sheet resistance, parallel resistance and capacitance of the $\text{MAPb}(\text{Br}_x\text{I}_{1-x})_3$ solar cells, as determined by modelling the high-frequency arc of the Nyquist plot.

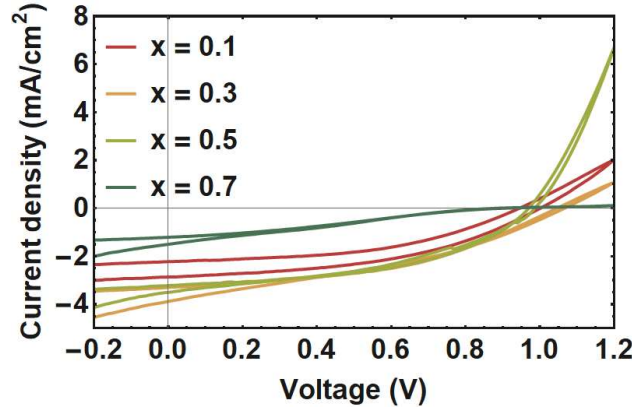


FIGURE 3.10. Light IV characterization of the $\text{MAPb}(\text{Br}_x\text{I}_{1-x})_3$ solar cell devices, measured with a scan speed of 10 mV.s^{-1} , for $x = 0.1, 0.2, 0.5$, and 0.7 .

To ensure that the TID measurements are non-destructive, once the TID measurement is finished, we repeat the impedance measurement, and verify that is unchanged with respect to the initial impedance measurement. To ensure measurement reproducibility, we either measure TID on multiple devices with the same composition or repeat the measurement multiple times on the same device.

Ion migration and hence phase segregation can happen under both the application of electrical or light bias. The voltage pulse in TID is a short perturbation after which we observe the drift of ions back to the steady-state position under zero bias. We assume that the properties of the ions (activation energy, density etc.) are independent of the applied bias for the mild electric fields applied here.

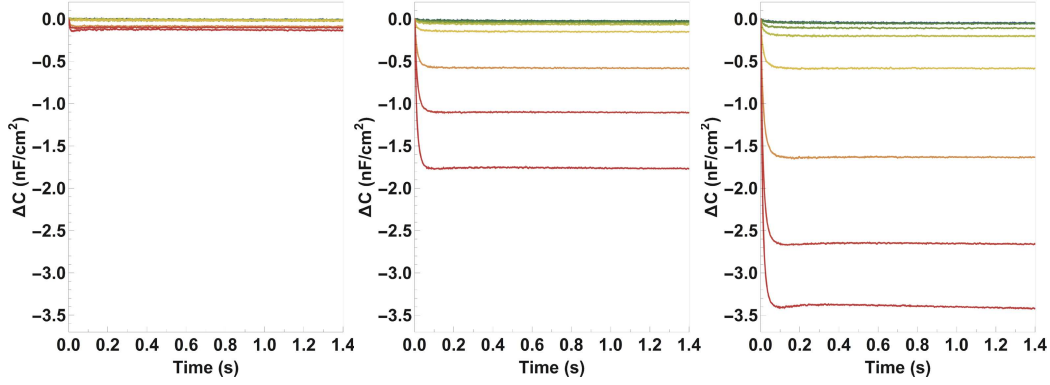


FIGURE 3.11. Relative difference in capacitance transients $\Delta C = C(t) - C_0$ of the MAPbBr_{0.3}I_{2.7} solar cell device, measured with an AC voltage of 20 mV, after applying a 2 s voltage pulse of (a) 1 V, (b) 1.25 V, and (c) 1.5 V, under dark conditions. The transients shown here are taken at temperatures of 210 K, 225 K, 240 K, 255 K, 270 K, 285 K, 300 K, 315 K and 330 K.

3.4.3 FITTING PROCEDURE

We use a global fit algorithm with the fit function shown in Equation 3.1. This fit function can be adapted to contain any number of exponential terms needed to resolve the full dataset of capacitance transients, where each of these exponential terms represents one specific ion migration process n , with its own ΔC_n , $p_{fit(n)}$ and $E_{a(n)}$.

The fitting procedure goes as follows: $C_\infty(T)$ is extracted from the measurements directly from the steady-state capacitance before we allow the algorithm to find the best value for $\Delta C(T)$ at each temperature and the best global values for p_{fit} and E_a . We thus directly obtain the value of the activation energy E_a . The fitted parameter p_{fit} is then used to determine the diffusion coefficient, using Equation 3.2:

$$D_0 = \frac{k_B \epsilon \epsilon_0}{q^2 N_D p_{fit}} \quad (3.2)$$

We further use Equation 3.3 below to obtain the temperature-dependent ion diffusion coefficient, $D(T)$.

$$D(T) = D_0 \exp\left(\frac{-E_a}{k_B T}\right) \quad (3.3)$$

In Figure 3.3b and e we present the diffusion coefficients calculated at room temperature, $D(300 \text{ K})$, for the MAPb(Br_xI_{1-x})₃ solar cells in dark and in light, respectively.

The fitted $\Delta C(T)$ parameter is used to determine the ion concentration N_{ion} , using Equation 3.4 below.

$$N_{ion}(T) = 2 N_D \frac{\Delta C(T)}{C_{\infty}(T)} \quad (3.4)$$

In Figure 3.3c,f, we present N_{ion} as a function of N_D and show the maximal value for the density of mobile ions, $N_{ion}(max)$.

On top of the set of assumptions detailed in Chapter 1 of this thesis, we note that we assume that the background doping does not change under illumination.

Values for the parameters in Figure 3.3 are obtained from multiple repetition of the fit procedure on the same TID transient, averaging the fit parameters giving the lowest chi-square values and taking their standard deviation as an estimate for the error.

We additionally note that in this Chapter, we attribute the ion migration to vacancy-mediated migration, as it has been suggested to be the most likely candidate process at play^{33,40}, and it is energetically favoured compared to interstitial-mediated ion migration³². Finally, we note that TID does not resolve the specific ion migration mechanism at play but is a powerful technique for quantifying the key ion migration characteristics mentioned above - E_a , D_{ion} , N_{ion} .